γ-ray emission in α-particle interactions with C, Mg, Si, and Fe at $E_\alpha = 50$–90 MeV

J. Kiener,[1,*] J. Bundesmann,[2] I. Deloncle,[1,*] A. Denker,[2] V. Tatischeff,[1,*] A. Gostojic,[1,†] C. Hamadache,[1,*] J. Röhrich,[2] H. Benhabiles,[3] I. Bourgaoub,[1] A. Coc,[1,*] F. Hammache,[4,*] R. Mezhoud,[3] and J. Peyré[1,*]

[1]*Centre de Sciences Nucléaires et de Sciences de la Matière (CSNSM), CNRS/IN2P3 et Université Paris-Sud, 91405 Orsay, France*
[2]*Protonen in der Therapie Helmholtz-Zentrum Berlin, Hahn-Meitner-Platz 1, 14109 Berlin, Germany*
[3]*Université de M'HAMMED BOUGARA de Boumerdès, Boulevard de l'indépendence 35000, Algeria*
[4]*Institut de Physique Nucléaire d'Orsay (IPNO), CNRS/IN2P3 et Université Paris-Sud, 91405 Orsay, France*

Nuclear deexcitation lines are regularly observed in the γ-ray emission spectra of strong solar flares. The most prominent lines are produced by interactions of protons and α particles, accelerated up to hundreds of MeV, with abundant nuclei of the solar atmosphere. Analysis and interpretation of these lines, which carry valuable information on the solar flare properties, need cross-section data for the γ-ray line emission in these interactions for a wide particle energy range. To this purpose, we measured the γ-ray emission in interactions of α-particle beams of $E_\alpha = 50$–90 MeV with target foils of C, Mg, Si, and Fe at the center for proton therapy of the Helmholtz-Zentrum Berlin. Setups of three high-purity Ge detectors and one LaBr$_3$:Ce detector have been employed to detect the γ rays in two experiment campaigns. Relatively large distances of the detectors from the target and pulsed beams with sub-ns-wide pulses allowed the separation of beam-induced prompt γ-ray emission from the targets from other γ rays and neutron-induced background. γ-ray production cross sections for about 60 deexcitation lines from excited target nuclei or reaction products have been determined. For the strongest deexcitation lines from the major target isotopes, ^{12}C, ^{24}Mg, ^{28}Si, ^{56}Fe, there are now measured cross-section data from reaction threshold to $E_\alpha = 90$ MeV that can be directly used for astrophysical applications like solar flares. Comparison of the results with a cross-section compilation for strong γ-ray lines in solar flare emissions and the predictions of the TALYS nuclear reaction code were done. They underline the importance of cross-section determinations at accelerator laboratories for the establishment of an accurate cross-section data base in a wide projectile energy range.

I. INTRODUCTION

Energetic particles are an important part of the interplanetary and interstellar medium and particle acceleration sites can be found throughout the Galaxy: in solar and stellar flares induced by violent magnetic reconnection, in supersonic shock waves from coronal mass ejections inside the heliosphere and from strong stellar winds, nova- and supernova explosions in the interstellar medium, and near compact objects like pulsars and black holes. Especially solar flares are known to accelerate protons, α particles and heavier nuclei in the corona up to several GeV per nucleon and electrons up to tens of MeV [1]. Part of these particles penetrate the solar atmosphere and induce γ-ray emission by interactions with the ambient matter. This has been regularly observed since 1972 during strong flares by γ-ray instruments in orbit.

The emission spectrum in the range of 100 keV to 10 MeV is characterized by prominent narrow γ-ray lines originating mostly from the deexcitation of the first few excited states of abundant nuclei in the solar atmosphere (^{12}C, ^{16}O, ^{20}Ne, ^{24}Mg, ^{28}Si, and ^{56}Fe), sitting above a quasicontinuum of thousands unresolved nuclear lines and a continuous component from electron bremsstrahlung. Intensity and shape of the lines and the continuum depend on the composition, spectra, and directional distribution of the accelerated particles and the abundances of the solar atmosphere. It can thus inform on the acceleration mechanism and the interaction site [2].

Ramaty, Kozlovsky, and Lingenfelter [2] first presented a comprehensive description of the emission of nuclear γ-ray lines in interactions of energetic protons and α particles with abundant nuclei and the inverse reactions in astrophysical sites. It included a first cross-section compilation for strong nuclear deexcitation lines emitted from solar flares and in interactions of galactic cosmic rays with interstellar matter as well as calculations of lineshapes. An update of this cross-section compilation was subsequently published by Kozlovsky, Murphy, and Ramaty [3], after many new cross-section data were determined in accelerator experiments.

The most recent compilation of Murphy, Kozlovsky, Kiener, and Share (MKKS) [4] includes a total of 243 cross-section curves with energies from reaction threshold to several hundred MeV per nucleon for proton, α-particle, and ^{3}He reactions. It relies on an impressive amount of measured γ-ray

---

production cross sections, mostly for energies below about 25 MeV for proton reactions and about 40 MeV for reactions with α particles. For the extrapolation to higher energies, as well as an assessment of the total γ-ray emission in a nuclear reaction including up to thousands of weaker lines, extensive calculations with the nuclear reaction code TALYS [5] were made.

An interesting feature was seen in the cross-section curves for α-particle reactions, especially for γ-ray lines coming from the deexcitation of the first few excited states of the abundant nuclei, i.e., the strongest lines in solar flares. Above the typical cross-section maximum in the range of $E_\alpha = 10$–20 MeV for inelastic scattering to the first-excited states in the abundant even-even nuclei cited above, TALYS predicted a second, broad cross-section maximum around $E_\alpha = 60$ MeV. This feature was recognized to come from fusion-evaporation reactions like (α, dnp), $(\alpha, n\,{}^3\mathrm{He})$, $(\alpha, 2n2p)$, etc. and would have a significant impact on the modeling and analysis of the strongest γ-ray lines in solar flares. However, practically no measured data for the γ-ray production in α-particle-induced reactions with the important nuclei exist above $E_\alpha \approx 40$ MeV.

We decided to measure γ-ray production cross sections for α-particle reactions with four of the important target nuclei in the energy range $E_\alpha = 50$–90 MeV to determine the importance of this second maximum. The experiment will be described in Sec. II, the data analysis in Sec. III, and the results obtained with the four targets are shown and discussed in Sec. IV. A short summary reviewing the most important results and perspectives concludes the paper.

II. EXPERIMENT

Data have been taken during two irradiation campaigns at the center for proton therapy of the Helmholtz-Zentrum Berlin (HZB) in 2015 and 2016. The pulsed α-particle beam of the cyclotron accelerator was directed onto self-supporting target foils mounted on a ladder inside a spherical stainless-steel target chamber of 15 cm diameter. This chamber had six tubes of 10-cm diameter, four of them connecting it to the beam line, pumping station, and target ladder setup. The two horizontal tubes perpendicular to the beam line were equipped with a 5-mm-thick glass window. A camera directed to look at the target position was installed at one of the glass windows and used for beam focusing with the help of a luminescent quartz on the target ladder.

In both irradiation campaigns, the same target foils of natural isotopic composition of C, Mg, Si, and Fe have been used. In 2016, we also used an Al foil. The target thickness has been determined at the Helmholtz Zentrum using their weight and area size. The results agreed with the values given by Goodfellow within less than 5% for all of them. An overview of their characteristics is given in Table I. The beam was stopped in a copper beam dump approximately 4 m downstream of the target chamber. Apart from the copper beam dump, the whole beam line structure was made of stainless steel. The high neutron and γ-ray flux caused by beam interactions with the copper towards the detectors was decreased by placing a lead wall and paraffin between the beam dump and the detectors.

TABLE I. Characteristics of the target foils used in the experiment, surface density ρ and atomic surface density N with uncertainties on the last digits in parentheses. The purity of all target foils exceeds 99%.

Element	ρ (mg/cm^2)	N (atoms/cm^2)	Remarks
			Flexible graphite,
C	8.86(44)	$0.444(22) \times 10^{21}$	Goodfellow
Mg	21.2(11)	$0.525(26) \times 10^{21}$	Goodfellow
Si	72.3(36)	$1.55(8) \times 10^{21}$	Si wafer
Fe	19.8(1.0)	$0.214(11) \times 10^{21}$	Goodfellow
Al	20.7(10)	$0.462(23) \times 10^{21}$	Goodfellow

Two different detection setups in 2015 and 2016 have been employed, consisting each of three high-purity Ge (HP-Ge) detectors and one LaBr$_3$ scintillation detector placed around the target chamber. In both setups, the detectors were positioned relatively far from the target, especially for the HP-Ge detectors, to obtain a good time-of-flight separation between neutrons and γ rays from reactions in the targets. The detectors covered a relatively large angular range with respect to the beam direction in order to determine γ-ray angular distributions. An overview of the characteristics of the employed detectors and their positions can be found in Table II.

In the first irradiation experiment, α-particle beams of $E_\alpha = 50$ MeV were directed onto the different target foils, with an intensity of $I_{\mathrm{beam}} \approx 2$ nA and a pulse rate of $f_b = 86.5$ kHz. Irradiation runs without targets were also done to measure the beam-induced background. The beam intensity was measured regularly in well-shielded Faraday cups (FCs) positioned directly behind the cyclotron and about 1 m upstream of the target chamber. The values of beam intensities taken by both FCs usually differed by less than 5%.

Beams of $E_\alpha = 60$, 75, and 90 MeV were delivered to the four different target foils in the second campaign. Runs without target were also done at each energy for background studies. Beam pulse rates were in the range of 400–900 kHz and intensities between 0.5 and 3 nA. Pulse widths of all α-particle beams in 2015 and 2016 were well below 1 ns. Beam intensities were determined in the same way as in the

TABLE II. Detectors used in the experiments: coaxial HP-Ge detectors and LaBr$_3$ detectors with cylindrical crystal. The dimensions are the crystal diameter Φ and length l. The distance is measured from the target position to the front face of the crystal housing.

Material	Manufacturer	Dimensions	Distance	Angle	Year
HP Ge	Canberra	55.5, 55 mm	76.5 cm	90°	2015
HP Ge	Eurisys	50.8, 52 mm	76.3 cm	116°	2015
HP Ge	PGT	42, 42 mm	57.8 cm	44°	2015
LaBr$_3$:Ce	Saint-Gobain	38.1, 38.1 mm	53.0 cm	151°	2015
HP Ge	Intertechnique[a]	71.5, 70 mm	57.6 cm	90°	2016
HP Ge	Ortec[a]	68, 72 mm	60.1 cm	147°	2016
HP Ge	Intertechnique[a]	69, 76 mm	52.6 cm	43°	2016
LaBr$_3$:Ce	Saint-Gobain	50.8, 50.8 mm	62.1 cm	76°	2016

[a]Detector from the IN2P3/STFC French-UK Ge pool [7].

2015 campaign using the same well-shielded FCs, and one additional FC that consisted of the last beam tube holding the copper beam dump, isolated from the rest of the beamline. The latter was less accurate, but was useful for a continuous monitoring of beam intensity.

To determine the detection efficiencies, a couple of runs with different radioactive sources have been recorded before, during, and after the beam irradiation runs. In 2015, radioactive sources of ^{137}Cs, ^{152}Eu, and ^{241}Am with activities of 165.5(83), 209.4(77), and 416.8(208) kBq, respectively, have been placed at the target position before and after the beam irradiations. After the beam irradiation runs, the HP-Ge detector was placed at a distance of 425 mm from the activated beam dump for determination of the detection efficiency curve in a more extended energy range than available from standard radioactive sources.

In addition to that, several measurements with a ^{60}Co source with an activity of 9.66(19) kBq, mounted onto the front faces of the detector crystal housing have been made at the HZB. After the experiment, measurements with ^{60}Co, ^{137}Cs, and ^{241}Am sources of 27.7(14) kBq, 3.45(17) MBq, and 427(21) kBq, respectively, at different distances on the detector axes were made at CSNSM Orsay. These runs at Orsay and those with ^{60}Co at HZB were done to determine the layout of the different detectors that were not always documented with the desired accuracy.

In the second irradiation campaign in 2016, ^{60}Co, ^{133}Ba, and ^{137}Cs sources of 7.83(15), 35.4(17), and 202(7) kBq, respectively, were placed at the target position. There have also been measurements with and without the glass window between the target and the HP-Ge detector sitting at an angle of 90°. Also, measurements with a ^{60}Co source of 22.4(11) kBq on and off axis were done at the CSNSM Orsay before and after the irradiations at HZB to determine the crystal layouts of the LaBr3 and the HP-Ge detectors.

Standard NIM electronic modules were used to process the detector signals. During the beam irradiation runs, an energy and timing signal was recorded in coincidence for each detector, but only the energy signal during the other runs. The timing signal was the time difference between the detector signal and the following pulse of the beam pulsation. Time delays were adjusted for each new α-particle beam, so that the peaks of prompt γ rays from the target and the beam dump were centered within a time window of 2 μs in 2015 and 0.5 μs in 2016.

For all data acquisitions at HZB and CSNSM, a MPA-3 system of FAST ComTec [6] with eight ADCs was used. It was equipped with an internal real-time clock, providing a time stamp with 50-ns resolution for each recorded event and a measure for the acquisition dead time for each ADC channel. All channels were set to 8 k resolution. The acquisition system provided also cumulated spectra of each ADC channel at the end of the run with 8 k resolution.

III. DATA ANALYSIS

For analysis, the list data of all beam irradiation runs were saved to data files having the tree structure format of ROOT, enabling fast and versatile data processing with ROOT appli-

cations [8]. Data of other runs without timing information, mostly calibration runs with radioactive sources, were directly taken from the ADC spectra created by the data-acquisition system.

A. Beam-charge determination

In all irradiation runs, beam currents in FCs at the cyclotron exit (FCJ2) or close to the target (FCTW2) were repeatedly noted, typically every 15–30 minutes. Both were well-shielded FCs with an estimated measurement uncertainty of 50 pA. Regular checks of the beam transmission from the cyclotron to the target chamber were also done by noting both FC values. They agreed to typically better than 5% for all beam currents down to $I_{beam} = 0.5$ nA. In the 2016 experiment, the FC at the end of the beam line was also operating with an estimated accuracy of $\Delta I_{beam} = 0.3$ nA. This FC agreed within this range with the values of FCJ2 and FCTW2. It was useful for a continuous monitoring of the beam intensity but was not used for the beam charge determination.

For the beam current integration, the necessary interpolation between the noted values of FCTW2 was done with the detector count rates. The latter were obtained by a sampling into 5-s bins of selected, time-stamped events. The selection englobed the visible strong peaks in the time spectra, which were formed by prompt γ rays and fast neutrons from beam interactions in the target and the beam dump. This minimized the background component not related to the instantaneous beam intensity, such as radiation from natural radioisotopes and activated materials. A residual constant background was subtracted from the obtained count rates. With this method, typical uncertainties for the beam charge Q_{run} were estimated at about 7%–15%, depending on the beam intensity.

B. Detection efficiencies

The full-energy detection efficiencies $\epsilon_{det}(E_\gamma)$ of the detectors in the 2015 and 2016 irradiation setups for the full range of interest, approximately 100–8000 keV, were obtained in two steps. First, from the runs with the radioactive sources at target position, $\epsilon_{det}(E_\gamma)$ was obtained in the range of $E_\gamma = $ 122–1408 keV in 2015 with the ^{137}Cs and ^{152}Eu sources. The 60-keV ^{241}Am line could only be observed in the Canberra detector sitting at 90°, facing the glass window of the target chamber. In the 2016 experiment, $\epsilon_{det}(E_\gamma)$ could be obtained in the range $E_\gamma = $ 81–1332 keV with ^{60}Co, ^{133}Ba, and ^{137}Cs sources.

Detection efficiencies $\epsilon_{det}(E_\gamma)$ in the full range were then obtained through detailed studies of the response function of the different detectors to incoming γ-ray line fluxes. For that, the high-statistics spectra measured at HZB and CSNSM with radioactive sources on and off the detector axes were compared with simulated spectra for those simple setups. The simulations were done with the GEANT simulation toolkit [9] by varying the uncertain parameters of the crystal layout. The most important one was the gap between the front face of the crystal housing and the crystal, not documented for most of the HP-Ge detectors. For some of the HP-Ge detectors, the precise crystal dimensions were also not known.
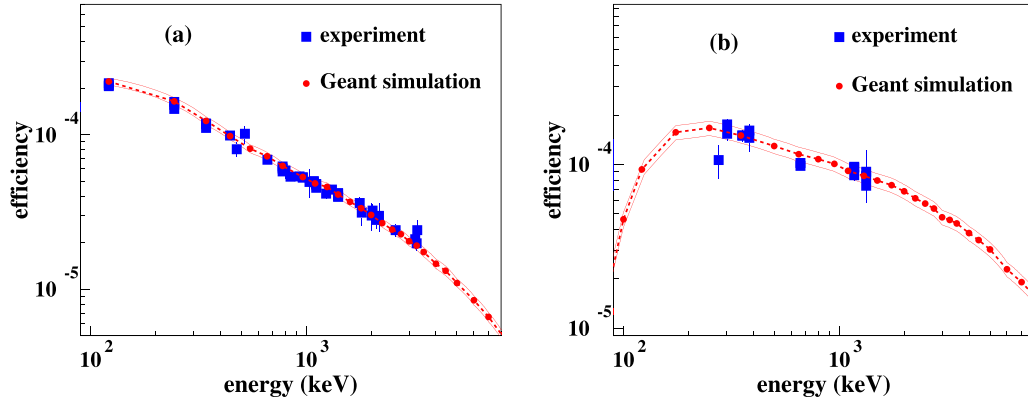
FIG. 1. Full-energy-peak detection efficiencies of HP-Ge detectors at $90°$ in the (a) 2015 and (b) 2016 campaign. Measured efficiency data with radioactive sources in the target chamber are shown by blue squares and simulated ones by red circles, connected with the dashed curve. The red upper and lower lines enclosing the simulation efficiencies represent the adopted uncertainty for the detection efficiency. For the HP-Ge detector in 2015, additionally to the standard radioactive sources, data from the decay of ^{55}Co and ^{56}Co in the activated beam dump could be obtained.

The best constraints were obtained from the on-axis measurements with ^{60}Co sources, done at 3–4 distances ranging from typically 4 mm to 15 cm. The crystal layout parameters in the simulations were varied, until an agreement of typically 3% was obtained between measured and simulated detection efficiencies for the 1173- and 1333-keV lines at all distances, as well as for the sum line at 2506 keV at the smallest distance. With these parameters, the detection efficiency curve for the irradiation setup in the full energy range was obtained from GEANT simulations [$\epsilon_{sim}(E_\gamma)$], normalized to the measured efficiencies with radioactive sources: $\epsilon_{det}(E_\gamma) = f_{sim} \, \epsilon_{sim}(E_\gamma)$. Figure 1 shows examples of simulated detection efficiency curves adjusted to the source measurements.

The uncertainties on the detection efficiency are essentially determined by the statistical uncertainties and the dispersions of the measured efficiency data around the normalized efficiency curves from the GEANT simulations. For the normalization factors f_{sim}, conservative estimates resulted in uncertainties of 5%–10%. This is in line with previous results obtained using a ^{56}Co source and the 992-keV resonance of the ^{27}Al(p, γ) reaction in addition to standard radioactive sources, extending the energy range of measured efficiency data to 10.7 MeV [10]. For the LaBr$_3$ detector in 2015 and the HP-Ge detector at $\Theta = 43°$ in 2016, absorption in a stainless-steel flange, depending on the exact position of the source or beam spot, was observed. For these two detectors, GEANT simulations with varying positions of the beam spot on the target inside a reasonable range were done. The difference between extreme values for absorption from the flange were used for the uncertainty calculations and quadratically added to the uncertainty on f_{sim}. It amounted to about 20% and 10% at $E_\gamma = 500$ keV for the LaBr$_3$ detector at $\Theta = 151°$ in 2015 and the HP-Ge detector at $\Theta = 43°$ in 2016, respectively.

C. Gamma-ray spectra

The γ-ray spectra of interest were created by extracting events inside the visible band in the time-energy histograms, coming from prompt γ rays induced by beam interactions in

the target. Definition of the contours containing the events of interest and their spectra was done using the ROOT data analysis framework. Figure 2 shows a zoom of a time-energy histogram around the prompt target γ rays, recorded with the LaBr$_3$ detector in 2016. For the LaBr$_3$ detectors, due to their excellent timing resolution, γ-ray spectra from interactions of secondary particles in the target chamber could also be
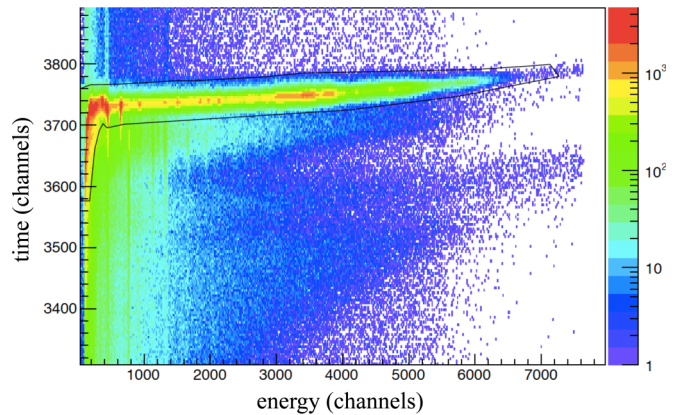
FIG. 2. Time vs energy histogram of events in the LaBr$_3$ detector from irradiation of the C target with 60-MeV α particles. The contour for prompt target γ rays is shown by the black line. The broad structure inside the contour at E2 $\sim$ 3000–4000 contains the full-energy and escape peaks of the 4.439-MeV line. Several other structures from narrow lines between E2 $\sim$ 150–3000 can also be distinguished. Below the contour a weaker band extends at T2 $\approx$ 3680, which is delayed by about 4 ns relative to prompt target γ rays. It contains several narrow γ-ray lines, nearly exclusively from ^{56}Fe and ^{52}Cr. These lines are most likely produced by interactions of secondary protons and neutrons in the target chamber walls and tubes. There is also some extension of these lines to longer delays, probably produced by the same particles in farther-away beam tubes and support structures. The large, vaguely triangular structure below T2 $\approx$ 3600 is from interactions of secondary neutrons in the detector crystal.
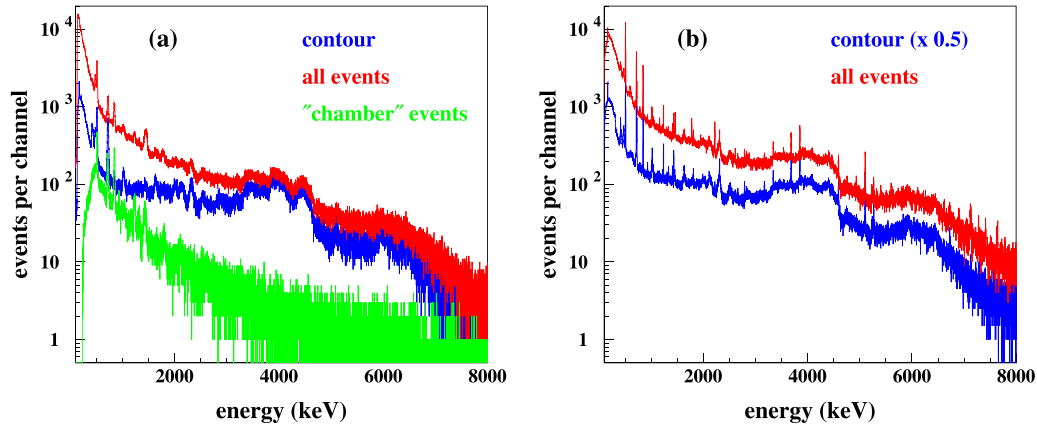
FIG. 3. γ-ray spectra recorded by the (a) LaBr$_3$ at $\Theta = 76°$ and the (b) HP-Ge detector at $\Theta = 90°$ during irradiation of the carbon target by a 60-MeV α-particle beam in the 2016 campaign. The blue lines show the spectra for events selected by the contour around the prompt γ rays from the target (see Fig. 2), red lines are the spectra for all events with energy and timing signal. The green line for the LaBr$_3$ detector are events dominated by interactions of secondary particles in the target chamber walls and tubes.

extracted. The strong γ-ray lines in these spectra, essentially from ^{56}Fe and ^{52}Cr, could be used for the energy calibration of the LaBr$_3$ detectors, which was not completely stable during the irradiation campaigns. The timing resolution of the HP-Ge detectors was not sufficient to completely separate these events from target γ rays. In some cases, relatively broad contours for HP-Ge detector data had to be defined, including also γ rays from interactions of secondary particles in farther away beam tubes and support structures.

Furthermore, spectra of all events with energy and timing signal were created for the LaBr$_3$ and the HP-Ge detectors. The comparison of intensities of some strong lines in these all-event spectra and the spectra of contour-selected events allowed a measure of the eventual loss of good events that was introduced by the contours. Another kind of spectra were from events with energy, but without timing signal. These spectra are dominated by radiation background, including long-lived activity produced during the irradiations and lines from thermal and epithermal neutron capture. In these spectra, several lines, in particular the strong 2223, 7631, and 7646 keV lines from neutron capture on H and Fe, respectively, were valuable for precise energy calibrations of the detectors in a wide energy range. Figure 3 shows examples of the different spectra for a LaBr$_3$ and a HP-Ge detector.

Finally, for some broad lines, especially the 4438-keV line of ^{12}C, the line integrals could only be obtained by a comparison with simulated line complexes including the Compton component and the escape lines, or from deconvolution of the spectra. The deconvoluted spectra were also very useful for the heavier targets, where many interesting lines were embedded in complex structures of overlapping lines, including escape lines. The necessary detector response functions for the deconvolution and/or the line-complex simulation were obtained by extensive GEANT simulations of the energy deposit in the detector crystals following the emission of γ rays from the beam spot on the target. These simulations were done for a wide range of γ-ray energies, $E_\gamma \approx 300$–7500 keV, with a comprehensive model of the experimental setup, including detailed descriptions of the target chamber, beam

line, detectors, and their support structures as well as floor and walls of the experiment room.

The capacity of these simulations to produce accurate detector response functions was checked by simulating detector spectra of γ-ray line emission with the branching ratios of a ^{152}Eu source and comparing them to measured spectra. An example of such a comparison is shown in Fig. 4 for the Eurisys HP-Ge detector in the 2015 campaign.

IV. RESULTS

Differential cross sections for the γ-ray angular distribution were obtained from the extracted line count integrals in the four detectors and the detection efficiencies, some
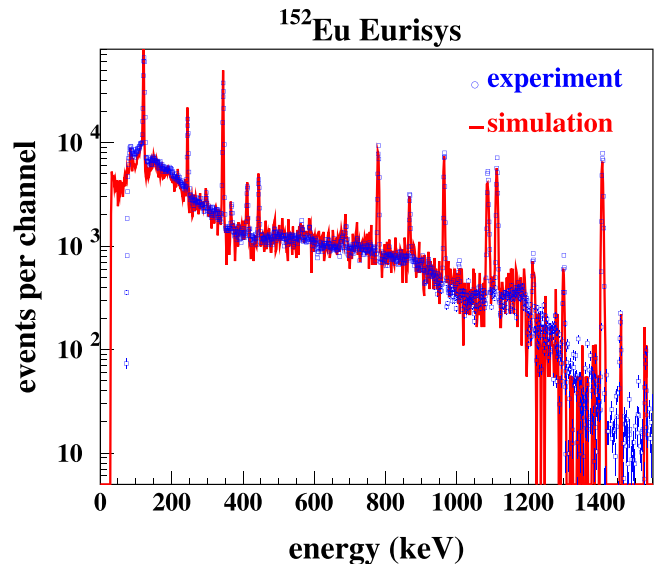
FIG. 4. Spectrum with a ^{152}Eu source at the target position, recorded by the Eurisys HP-Ge detector (blue symbols) and GEANT simulation with a detailed model of the experimental setup and all ^{152}Eu decay lines with branching ratio >0.1% (red line).
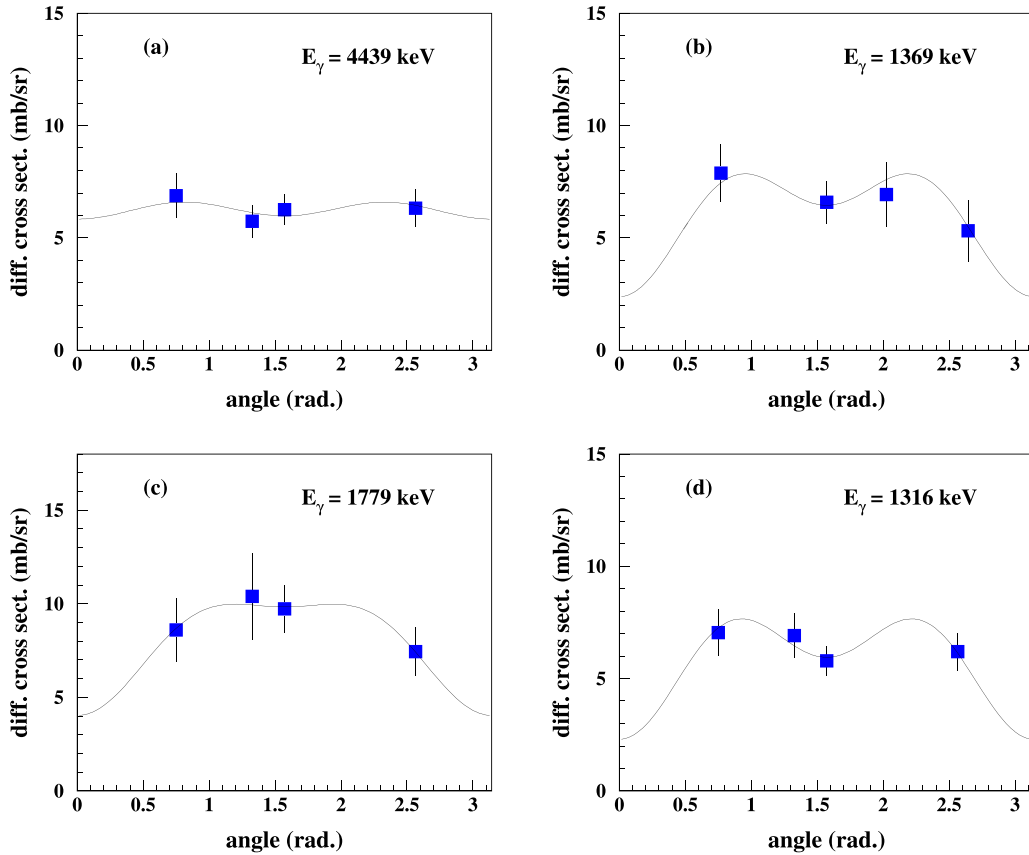
FIG. 5. Examples of measured differential γ-ray emission cross sections (blue symbols) and Legendre-polynomial fits (black lines). Data from (a) irradiation of the C target at $E_\alpha = 75$ MeV, (b) irradiation of the Mg target at $E_\alpha = 50$ MeV, (c) irradiation of the Si target at $E_\alpha = 60$ MeV, and (d) irradiation of the Fe at target $E_\alpha = 90$ MeV, the γ-ray line energies being indicated on the figures.

examples are displayed in Fig. 5. Count integrals were obtained by simple line integration or fits in the cases of isolated, narrow lines or in more complicated cases like overlapping or very broad lines by multiline fits and comparison with simulated line complexes, as explained above. A lot of effort was put into the extraction of integrals for the strongest lines in the spectra of each target, and for lines where cross-section data exist at lower α-particle energies. The γ-ray line emission cross sections were then obtained by Legendre-polynomial fits of the γ-ray angular distribution data:

$$W(\Theta) = \sum_{l=0}^{l=l_{\max}} a_l Q_l P_l(\cos\Theta) \ (l \text{ even}), \quad (1)$$

with $l_{\max}$ being twice the γ-ray transition multipolarity and Q_l the attenuation coefficients, which in the present setup differ from 1 by less than 5×10^{-3}. The coefficient a_0 is directly proportional to the angle-integrated cross section. Reduced χ^2 of the fits were in most cases well below unity, and very rarely exceeded two, indicating correct or slightly overestimated values for the uncertainties on the differential cross section data from detector efficiencies and the line integral determinations. For several lines, in particular from measurements with the Fe target, only three data points from the HP-Ge detectors were available, which is just sufficient to determine the a_l coefficients for electric quadrupole transitions, resulting in

increased cross-section uncertainties. A similar situation was found for the 6.13-MeV line of ^{16}O, whose electric octupole transition to the ground state required the determination of four coefficients with the four detector data.

For the final uncertainties of the integrated cross sections, uncertainties from the target thickness and the beam-charge determination were quadratically added to the uncertainty resulting from the Legendre-polynomial fits. It results for strong, isolated lines in final uncertainties of the order of 15%, while for weaker lines or lines embedded in complex structures these uncertainties may reach 30%–40%. An overview of the different uncertainties is given in Table III.

For the calculations with the TALYS nuclear reaction code, we used the most basic input, meaning only the target and projectile A and Z and the kinetic energy is given in the

TABLE III. Uncertainties entering the cross-section determinations, see text for more details.

Determined quantity	Uncertainty (%)	Remarks
Count integral	5–50	Includes dead-time corrections
Detection efficiency	5–20	Energy dependent
Beam charge	5–15	
Target thickness	5	
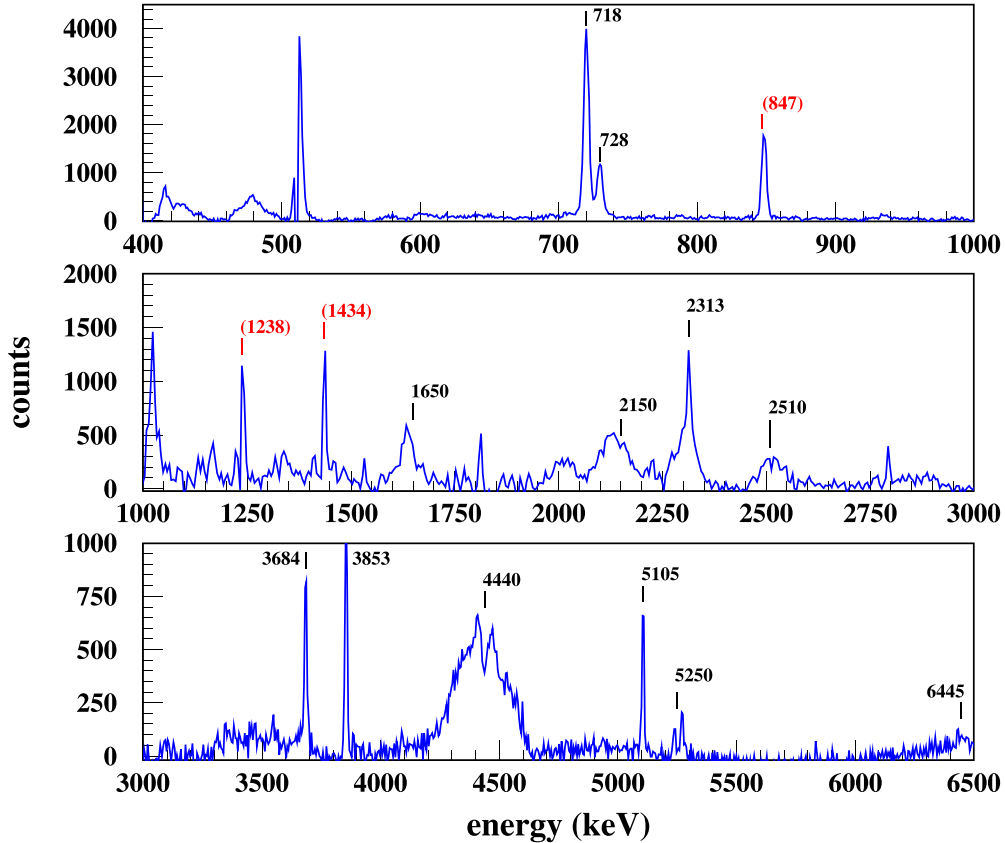
FIG. 6. Compton-suppressed spectrum of the HP-Ge detector at $\Theta = 90°$ from the irradiation of the C target with 60-MeV α particles in the 2016 experiment with 1-keV/channel resolution below 1 MeV and 5-keV/channel resolution above. The lines listed in Table IV are marked with their energy in keV, as well as lines due to interactions of secondary particles in the chamber walls and tubes (red numbers in parentheses).

input. We changed, however, the levels data base for nuclei with $A \leqslant 60$. In the version that we used (TALYS-1.6), the experimentally known levels are exclusively depopulated by electromagnetic transitions. For levels above the p, n, and α-particle emission thresholds, the gamma-decay branchings were modified to take account of the particle decay. We restricted also the number of discrete states (discrete states in TALYS are the experimentally known levels) in the calculations accordingly. These calculations are labeled in the following with "default parameters."

A. Lines from the C target

By far the strongest line feature at all projectile energies with the carbon target is a broad line around 4.44 MeV, whose major component is the 4439-keV line of ^{12}C. Other broadened lines of some importance are close to 6.4, 2.5, 2.3, 2.1, and 2.0 MeV and 1.65 MeV, as can be seen in Fig. 6. Many of these line features have several components, which are detailed in Table IV for those where cross sections have been extracted. Also, several narrow lines are clearly visible, the strongest one being the 718.35-keV line of ^{10}B, partly overlapping with the 728.34-keV line of ^{14}N. The lines close to 0.85 and 1.25 MeV are the 847- and 1238-keV lines of ^{56}Fe, produced by scattered projectiles and secondary particles in

the target chamber and beam tube structures. The line close to 1.45 MeV is partly from the 1436-keV line from ^{10}B, but is contaminated by a line at 1434 keV from ^{52}Cr, having probably the same origin as the ^{56}Fe lines. Table IV presents the list of lines and line complexes for which γ-ray emission cross sections have been obtained.

1. The 4.44-MeV line complex

The measured cross sections for the broad line at 4.44 MeV in the two experiments at Berlin, together with previous data and results of calculations with the TALYS nuclear reaction code [5], are shown in Fig. 7. Below 25 MeV, the 4439-keV line of ^{12}C is the only component, while sizable contributions of other lines are predicted above $E_\alpha = 35$ MeV by the TALYS calculations. The most important one is the 4445-keV line of ^{11}B, smaller contributions come from the 4319- and 4339-keV lines of ^{11}C above $E_\alpha = 40$ MeV. The present data show an indication of the second cross-section maximum around 70 MeV due to fusion-evaporation reactions, predicted in the compilation of MKKS [4] and in the TALYS calculations. Interestingly, the TALYS calculations reproduce remarkably well the cross section curve up to about 25 MeV and above 60 MeV. Between these energies, however, the calculations clearly underestimate the experimental data.

TABLE IV. γ-ray lines in α-particle reactions with the C target for which cross sections have been obtained. The first column designs the energy of the γ-ray line or the approximate mean energy of the line complex. See Supplemental Material [25] for numerical values of the cross sections.

E_{line} (keV)	Main component	Other components	Remarks
6445	^{14}N, 6446.17 → g.s.		
5250	^{15}N, 5270.155 → g.s.	^{15}O, 5240.9 → g.s.	
5105	^{14}N, 5105.89 → g.s.		
4440	^{12}C, 4439.82 → g.s.	^{11}B, 4444.98 → g.s.	
		^{11}C, 4318.8 → g.s.	
3853	^{13}C, 3853.7 → g.s.	^{14}N, 6203.5 → 2312.8	
3684	^{13}C, 3684.5 → g.s.		
2510	^{14}N, 6446.17 → 3948.10	^{14}N, 8964 → 6446.17	
2313	^{14}N, 2312.593 → g.s.	^{15}N, 7567.1 → 5270.155	
2150	^{11}B, 2124.693 → g.s.	^{10}B, 2154.27 → g.s.	
		^{11}C, 6478.2 → 4318.8	
2100		^{11}C, 2000.0 → g.s.	Line complex 2.0–2.2 MeV
		^{15}O, 7275.9 → 5240.9	Add components listed in
		^{15}N, 9154.9 → 7155.05	$E_{\text{line}} = 2150$ keV
1650	^{14}N, 3948.10 → 2312.593	^{15}O, 6859.4 → 5240.9	
		^{12}B, 1673.65 → g.s.	
		^{12}B, 2620.8 → 953.14	
728	^{14}N, 5834.25 → 5105.89		
718	^{10}B, 718.380 → g.s.		

Because the 4.44-MeV line has an outstanding importance in solar-flare γ-ray emissions, we tried to understand this behavior and the composition of the line. An important part of the discrepancy in the $E_\alpha = 30$–50 MeV range between the data and the TALYS calculation is due to large cross-section differences for the inelastic scattering off ^{12}C. This can be
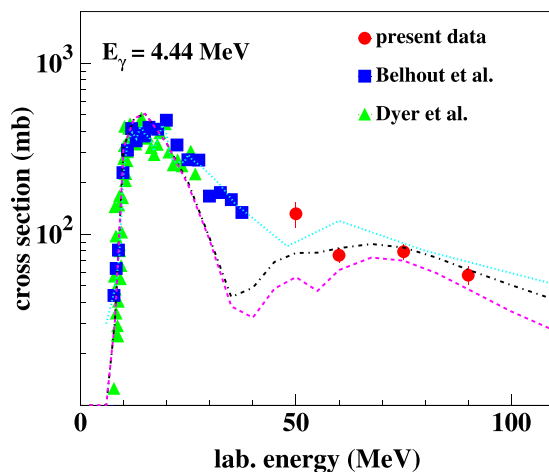
FIG. 7. Cross section for emission of the 4.44-MeV line in α-particle reactions with natural carbon targets in the present experiment and in Belhout *et al.* [10] and with enriched ^{12}C targets in Dyer *et al.* [11]. The dotted cyan line shows the values of the MKKS compilation [4], the dot-dashed black line is the result of calculations with the TALYS-1.6 code [5] with default parameters, including γ-ray lines in the window $E_\gamma = 4439 \pm 140$ keV, while the dashed magenta line shows the contribution of the 4439-keV line of ^{12}C.

deduced from measured differential cross sections $d\sigma/d\Omega_\alpha$ for ^{12}C$(\alpha, \alpha')^{12}$C$^*_{4.440}$. Integration of the measured $d\sigma/d\Omega_\alpha$, with missing angular ranges complemented by nuclear reaction calculations, at $E_\alpha = 32.5$, 36, 41, and 51 MeV from Refs. [12–15] yields cross sections values of 140, 126, 94, and 65 mb, respectively, while the prediction of TALYS at $E_\alpha = 30$, 40, and 50 MeV is 92, 22, and 14 mb, respectively.

An analysis of the lineshapes at $\Theta = 90°$ indicates also an important contribution of the inelastic-scattering component, as shown on Fig. 8. The calculated lineshapes for the inelastic scattering have been obtained with nuclear reaction calculations in the coupled channels framework. For the latter, the program ECIS [16] has first been used to fit the available inelastic-scattering data. For these fits, the 0^+ ground state, the 4.440-MeV 2^+ state, and the 14.08-MeV 4^+ state have been rotationally coupled, and the parameters of the nuclear reaction potential were varied until a satisfactory description of the experimental data has been obtained. The results of the ECIS calculations were then used to calculate the lineshape of the 4.439-MeV γ-ray line, following the method described in Ref. [17].

For the contributions of the 4445- and 4319-keV lines of ^{11}B and ^{11}C, respectively, we assumed fusion-evaporation reactions with a sequential emission of an α particle followed by a nucleon. The angular distribution of the emitted α-particle was taken from ^{12}C(α, α') angular distributions predicted by TALYS for ^{12}C states above the particle emission threshold. We took also from TALYS the mean excitation energies of these states, otherwise we assumed isotropic emission of the nucleon and the subsequent γ-ray in the frame of the emitting nuclei. The shape of the fusion-evaporation component of the 4439-keV γ ray of ^{12}C in reactions like $(\alpha, n\,^3$He$)$ or (α, dpn) is very similar to that of the 4445-keV line of ^{11}B and was
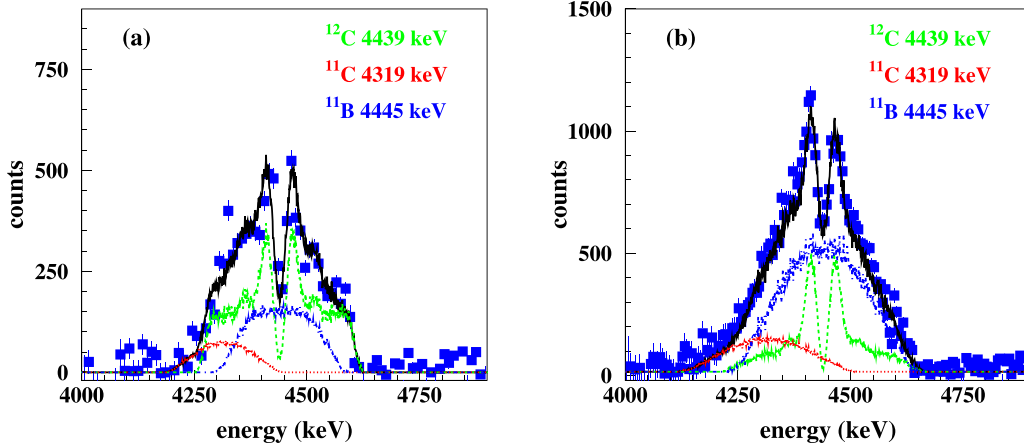
FIG. 8. Symbols show the 4.44-MeV line complex in Compton-suppressed spectra of the Ge detectors sitting at $\Theta = 90°$ for (a) $E_\alpha = 50$ MeV and (b) $E_\alpha = 75$ MeV. The different lines show calculated lineshapes for the 4439-keV line of ^{12}C from inelastic scattering (dashed green), the 4319-keV line of ^{11}C (dotted red), and the 4445-keV line of ^{11}B (dot-dashed blue), the solid black line showing the sum of the calculated lines. Inelastic scattering off ^{12}C accounts here to about 60% and 30% of the line complex at $E_\alpha = 50$ and 75 MeV, respectively.

therefore not explicitly included, while the 4339-keV line of ^{11}C was not necessary to describe the lineshapes.

The cross sections for inelastic scattering to the 4.440-MeV state determined in the lineshape analyses at $E_\alpha = 50$, 60, 75, and 90 MeV and the one from the inelastic-scattering angular distributions at $E_\alpha = 51$, 65, 72, and 90 MeV (see Refs. [15,18–20]) agree to better than 30%, which is compatible with estimated uncertainties. The TALYS predictions for inelastic scattering to the 4.440-MeV state are by factors of about three to eight below these values. This is compensated in TALYS by stronger contributions from fusion-evaporation reactions for the 4439- and 4445-keV lines, reaching a good agreement with the actual data for the 4.44-MeV line above $E_\alpha = 60$ MeV. Such a behavior comes probably from the use of a global nuclear reaction potential in TALYS, that may not be well adapted to light nuclei like ^{12}C. In fact, using the potentials obtained with ECIS in the above-described fits in TALYS improves considerably the overall agreement of TALYS calculations with the different components of the 4.44-MeV line complex.

To summarize, the cross section curve of the 4.44-MeV γ-ray line in α-particle reactions with C is now experimentally well defined from threshold up to $E_\alpha = 90$ MeV. It was shown that coupled-channels calculations for inelastic scattering leading to the emission of 4439-keV γ rays together with simple assumptions for fusion-evaporation reactions for the 4319- and 4445-keV lines of ^{11}C and ^{11}B, respectively, lead to a very good reproduction of the lineshapes at $\Theta = 90°$. This is very encouraging for comprehensive lineshape calculations, which should cover the complete γ-ray emission angular range in a wide α-particle energy range, similar to the work presented in Ref. [17] for the $p + {}^{12}$C reaction. The extrapolation of the cross section to higher energies can probably also be improved with the use of new $\alpha + {}^{12}$C nuclear reaction potentials obtained in fits of existing inelastic scattering data for $E_\alpha \geqslant 100$ MeV. This has, for example, been shown to give good results for proton reactions with Mg, Si, and Fe in a similar energy range [21].

2. Other lines from the C target

Cross sections for several other γ-ray lines that are present in the compilation of MKKS are shown in Fig. 9. Both the compilation of MKKS and the TALYS calculations describe only approximately the experimental data. In the MKKS compilation, previous data from Dyer *et al.* [11] and Belhout *et al.* [10] for the 5250-keV line have been included, the curve follows therefore closely the data up to $E_\alpha = 40$ MeV. Above that energy, the compilation overestimates the present data by about a factor of two. For the other lines, the data of Belhout *et al.* were apparently not considered in the compilation and the agreement of the compilation with the data is similar or worse and the energy dependence of the data is generally not correctly reproduced. The TALYS calculations with default parameters are not better in predicting the absolute magnitude and energy dependence of the data than the compilation. Unfortunately, the use of the new potentials in TALYS, as described above for the 4.44-MeV line, hardly improved the agreement with the data of other γ-ray lines from $\alpha + {}^{12}$C reactions.

The present results clearly show the importance of measurements to obtain reliable and precise cross-section data in a wide energy range. For the $\alpha + {}^{12}$C reaction, cross-section data for the dozen strongest γ-ray lines are now available from threshold to $E_\alpha = 90$ MeV. This is already sufficient for analysis of solar flare γ-ray emissions, where the particle spectra are often relatively soft and nuclear γ-ray line emissions occur mainly for particle energies below about 20 MeV per nucleon. An improvement with respect to the MKKS compilation in extrapolations to higher energies needs probably a detailed analysis of the different nuclear structure parameters in TALYS affecting the γ-ray emission cross sections in the $\alpha + {}^{12}$C reaction.

B. Lines from the Mg target

Figure 10 shows a spectrum of the Mg target at $E_\alpha = 60$ MeV, where a dozen relatively strong narrow lines and
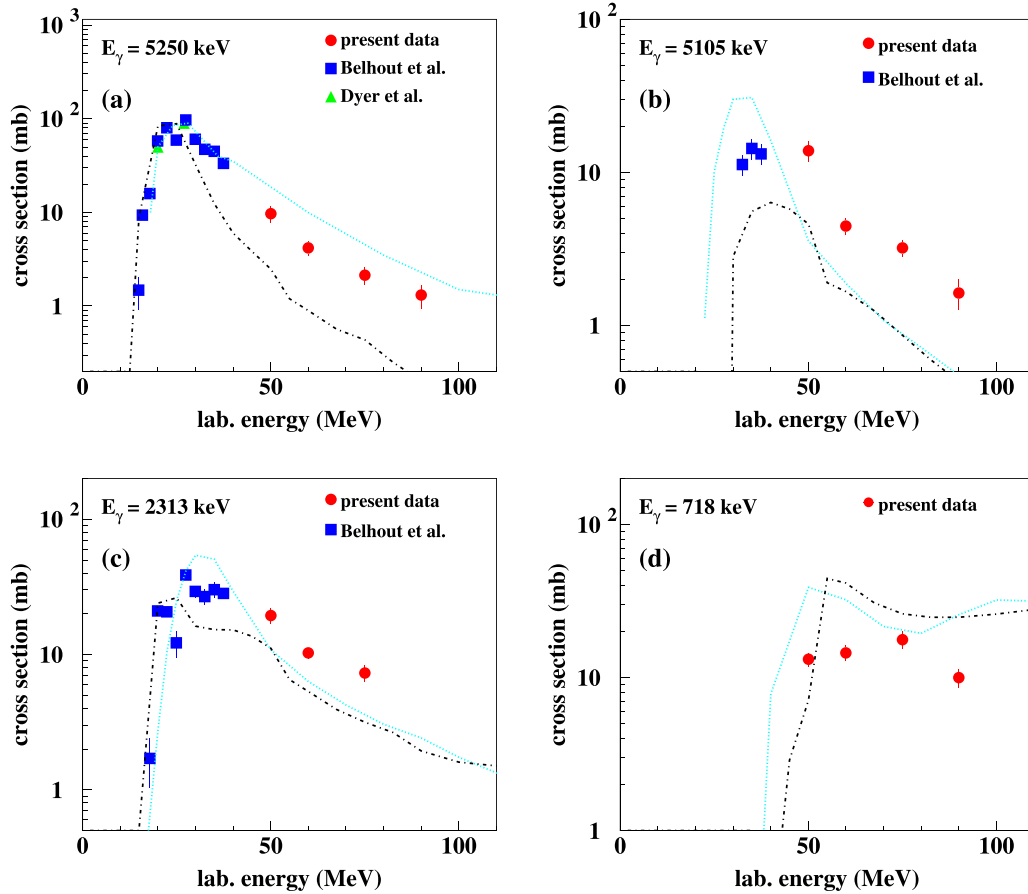
FIG. 9. Symbols show measured cross-section data for four different lines emitted in α-particle reactions with C (see Fig. 7 for more details). γ-ray line energies indicated in the panels refer to the lines listed in Table IV. The dotted cyan line show the values from the cross-section compilation [4] and the dot-dashed black lines are the results of TALYS calculations.

several complex and broad line features can be observed. The most prominent narrow lines are at 351, 440, and 1369 keV from ^{21}Ne, ^{23}Na, and ^{24}Mg, respectively. The strongest

features, however, are the line complexes in the 1300–1800 keV range, which include the 1369-keV line of ^{24}Mg, the 1634-keV line of ^{20}Ne, and the 1809-keV line of ^{26}Mg. All are

TABLE V. γ-ray lines in α-particle reactions with the Mg target for which cross sections have been obtained. The first column designs the energy of the γ-ray line or the approximate mean energy of the line complex. See Supplemental Material [25] for numerical values of the cross sections.

E_{line} (keV)	Main component	Other components	Remarks
6129	^{16}O, 6129.89 → g.s.		
2754	^{24}Mg, 4122.889 → 1368.672	^{25}Mg, 4711.6 → 1964.6	
		^{23}Mg, 2771 → g.s.	
1800	^{26}Mg, 1808.74 → g.s.	Many lines in	$E_\gamma = 1750$–1830 keV
1634	^{20}Ne, 1633.674 → g.s.	^{23}Na, 2076.011 → 439.990	
1369	^{24}Mg, 1368.672 → g.s.	^{22}Na, 1951.8 → 583.05	
891	^{22}Na, 890.89 → g.s.		
585	^{25}Mg, 585.045 → g.s.		
583	^{22}Na, 583.04 → g.s.		
451	^{23}Mg, 450.71 → g.s.		
440	^{23}Na, 439.990 → g.s.		
417	^{26}Al, 416.852 → g.s.		
390	^{25}Mg, 974.756 → 585.045		
351	^{21}Ne, 350.727 → g.s.		
332	^{21}Na, 331.90 → g.s.		
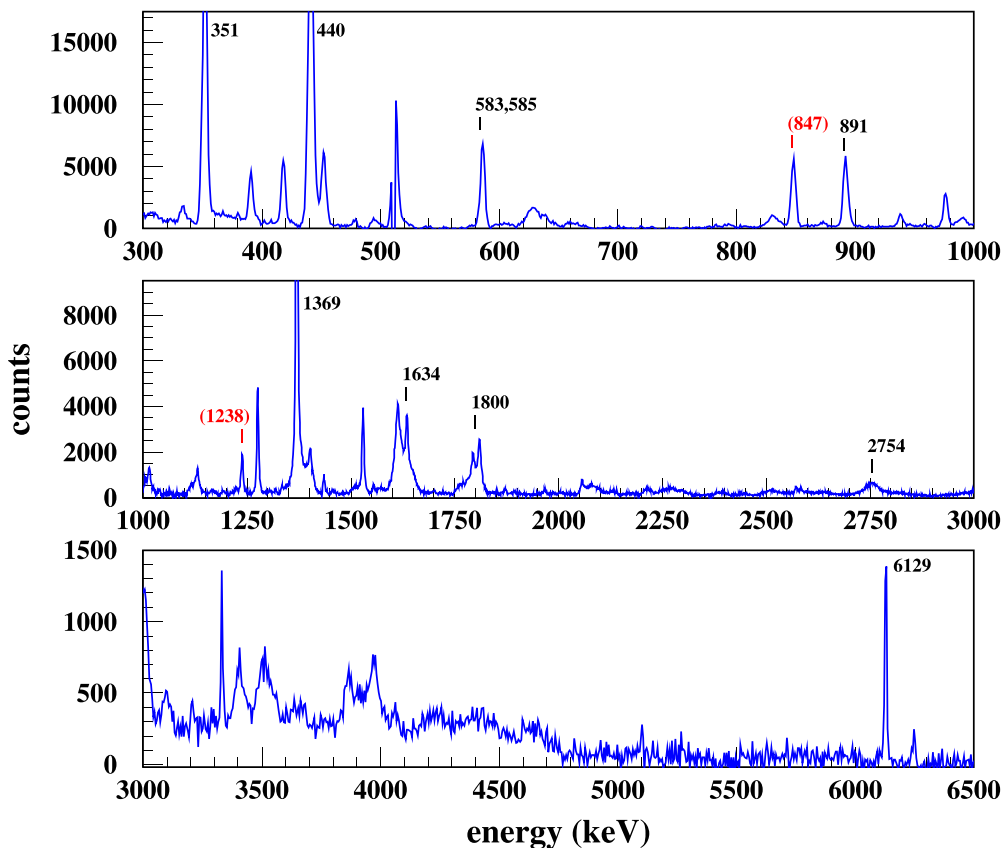
FIG. 10. Compton-suppressed spectrum of the HP-Ge detector at $\Theta = 90°$ from the irradiation of the Mg target with 60-MeV α particles in the 2016 experiment in 1-keV/channel resolution below 3 MeV and 5-keV/channel resolution above. A selection of strong lines listed in Table V are marked with their energy in keV, as well as lines due to interactions of secondary particles in the chamber walls and tubes (red numbers in parentheses).

overlapping with other relatively strong lines and the determination of cross sections there was only possible with detailed lineshape analysis. Examples for the 1.37- and 1.63-MeV line complexes are presented in Fig. 11.

The calculations for all lines in these two complexes, with the exception of the 1369-keV line of ^{24}Mg, were done by assuming fusion-evaporation reactions. In reactions producing lines from nuclei lighter than ^{24}Mg, the first emission was
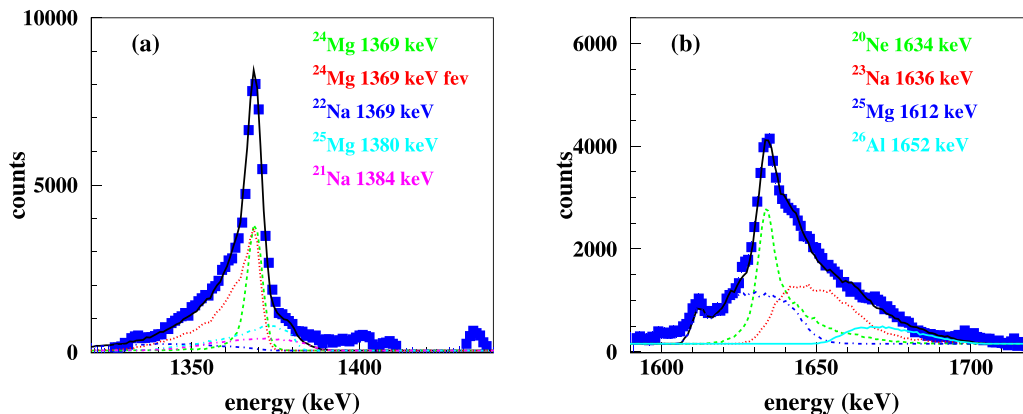
FIG. 11. Symbols show (a) the 1.37-MeV line complex in Compton-suppressed spectra of the Ge detectors sitting at $\Theta = 147°$ for $E_\alpha = 75$ MeV and (b) the 1.63-MeV line complex at $\Theta = 43°$ for $E_\alpha = 60$ MeV. The dashed, dotted, and dot-dashed lines show calculated lineshapes for the strongest components. The sum of all components is shown by the solid black lines. Two separated calculations were done for the 1369-keV line of ^{24}Mg, one for the inelastic-scattering component, and one for the fusion-evaporation component, labeled "fev" in panel (a).

assumed to be an α particle, followed by isotropic emission of one or more nucleons and the γ ray. For the other nuclei, sequential emission of two particles like, for example, $d + p$ for ^{25}Mg was assumed, again with isotropic emission of the second particle. Parameters for the lineshape calculations, like angular distributions for emission of the first particle, and emission energies were taken from TALYS calculations.

The 1369-keV line of ^{24}Mg received some special attention because of its importance in solar flare emission and its 1.33-ps half-life, which leads to an important emission component from slowed-down or stopped ^{24}Mg recoil nuclei. For the inelastic-scattering component, differential cross sections $d\sigma/d\Omega_\alpha$ of TALYS were used, which reproduce quite accurately the available data at $E_\alpha = 50$, 66, and 81 MeV of Ref. [22], while the γ-ray emission was assumed isotropic for the sake of simplicity. Here, the predominance of small scattering angles leads to mostly low energies of the recoiling ^{24}Mg and consequently to a relatively featureless narrow line, while calculations for the fusion-evaporation component lead to more extended lineshapes. This is illustrated by the dotted red and dashed green lines in Fig. 11(a).

Lineshape analysis for γ-ray lines embedded in such broad and complex features induced significant cross-section uncertainties. This is in particular true for the 1634-keV line where those uncertainties were on the order of 30%. It was still more difficult to determine cross sections for the 1809-keV line of ^{26}Mg because of important contributions of reactions not only with ^{24}Mg, but also with the minor isotopes ^{25}Mg (10.0%) and ^{26}Mg (11.0%). Furthermore, the intermediate half-life $t_{1/2} = 430$ fs of the emitting level and important feeding by cascades from higher-lying levels with similar or longer half-lives, lead to significant uncertainties for the γ-ray emission during the slowing-down phase of the recoiling ^{26}Mg. We decided therefore to determine cross sections only for the whole line complex extending from $E \approx 1.75$ MeV to ≈ 1.83 MeV at $\theta = 90°$.

The other lines for which cross sections were extracted are narrow lines from excited states with half-lives generally exceeding a few ps, where the emission happens essentially at rest. A special treatment was applied to the lines at 583.04 and 585.045 keV of ^{22}Na and ^{25}Mg, respectively. Even with the high-resolution HP-Ge detectors they were blended into a single line in our spectra. Their very different half-lives $t_{1/2} = 3.38$ ns (583.04 keV) and 243 ns (585.028 keV), however, were visible in the line intensity as a function of time since the beam pulse. Cross sections were then determined by fits of those time profiles with the two known half-lives.

A selection of measured cross-section data for strong lines from the present and previous experiments is shown in Fig. 12, together with cross sections from the compilation [4] and TALYS calculations with default parameters. The compilation follows naturally the data of Seamster *et al.* [23] and Belhout *et al.* [10] but seems to not have included the data of Belhout *et al.* for the 1634- and 585-keV lines. The present data show a hint of the second cross-section maxima for three lines in the range of $E_\alpha = 60$–90 MeV, but the cross sections are significantly smaller than the predictions from the compilation. The TALYS calculations reproduce reasonably well the

cross-section curves up to $E_\alpha \approx 50$ MeV but, like the compilation, overestimate the cross sections above that energy. A similar behavior can also be observed for the other lines listed in Table V.

C. Lines from the Si target

The spectra taken with the Si target show some similarities with the spectra from the Mg target. In Fig. 13 one can see a dozen strong narrow lines above $E = 0.3$ MeV and also several strong broad or complex structures, especially in the range of $E = 1$–3 MeV. The strongest line is the 1779-keV line of ^{28}Si, which is partially overlapping with the 1809-keV line of ^{26}Mg. There are a dozen weaker lines that may contribute to the 1779-keV line, but only the three lines listed in Table VI have contributions exceeding the few-percent level in the range of $E_\alpha = 50$–90 MeV in TALYS calculations.

Other strong lines with cross sections exceeding 25 mb at $E_\alpha = 60$ MeV are at 1273, 1595.5, and 2028 keV from ^{29}Si, 2838 keV from ^{28}Si, and 440 keV from ^{23}Na. Cross sections for these strong lines have been extracted, as well as for a line at 1.27 MeV, for which Seamster *et al.* [23] measured cross sections at lower α-particle energies. All of them are overlapping with one or more relatively strong lines, requiring lineshape analysis for the determination of cross sections, with a method very similar to that employed for the $\alpha + $ Mg reactions described above. Additionally, cross sections for several other lines of ^{28}Si were extracted, representing at least one transition for each of the seven lowest excited states. We tried also to extract cross sections for the line complex of the 2234- and 2235-keV lines of ^{31}P and ^{30}Si with important cross sections below $E_\alpha = 26$ MeV, which have been determined by Seamster *et al.* It was impossible to extract reliable values from the broad line complex in which it was embedded. Examples for the 1.27-MeV and 1.78-MeV line complexes are shown in Fig. 14. The list of lines for which cross sections have been determined is given in Table VI.

Figure 15 shows cross sections from the present experiment for four strong lines together with the cross-section curves of the compilation [4] and from calculations with TALYS. The data of Seamster *et al.* [23] for the 1779- and 1265-keV lines are also shown. The second cross-section maximum at $E_\alpha \approx 70$ MeV is clearly visible for the 1779-keV line of ^{28}Si and is also clearly present in the 2838-keV line from the second-excited state of ^{28}Si. For lines from other states of ^{28}Si listed in Table VI, there is an indication of the maximum where cross-section data could be determined for at least three different energies. TALYS calculations and the cross-section compilation show approximately the shape of this feature, but typically reach only a factor of two in magnitude. The same holds for lines from other residual nuclei that are produced in the reactions. Absolute cross-section values from the calculations and the compilation are typically within a factor of two of the measured data while the energy dependence is approximately reproduced.

D. Lines from the Fe target

The γ-ray spectra obtained with the Fe target from HP-Ge detectors are characterized by a dozen of relatively strong,
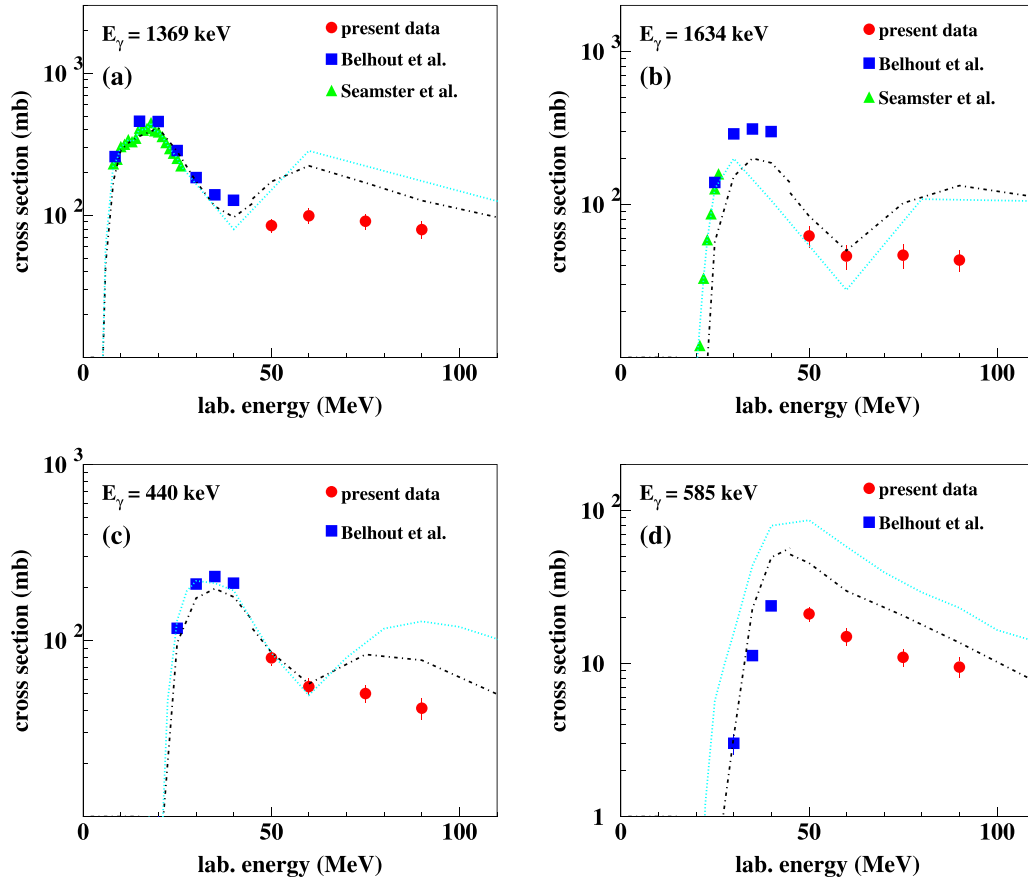
FIG. 12. Symbols show measured cross-section data for four different lines emitted in α-particle reactions with natural Mg target from the present experiment, and with enriched ^{24}Mg targets from Belhout *et al.* [10] and Seamster *et al.* [23]. γ-ray line energies indicated in the panels refer to the lines listed in Table V. The dotted cyan lines show the values from the cross-section compilation [4] and the dot-dashed black lines are the results of TALYS calculations. TALYS cross sections up to 45 MeV are the results for a ^{24}Mg target, and above 45 MeV for a natural Mg target.

narrow peaks below $E_\gamma \approx 1.5$ MeV (see Fig. 16). Above that energy are several moderately strong, narrow peaks visible up to ≈ 3.5 MeV followed by an essentially structureless continuum at higher energies. The strongest line in the range $E_\alpha = 60$–90 MeV is the 847-keV line of ^{56}Fe from its first-excited state ($J^\pi = 2^+$), closely followed by the 1223-keV line and the 1238-keV line from the second excited state (4^+) of ^{56}Fe. For these three lines, the cross-section maximum exceeds 150 mb and even 200 mb for the 847-keV line at $E_\alpha = 60$ MeV. At $E_\alpha = 50$ MeV, the 1223-keV line has the highest cross section. TALYS calculations show that it is dominated at this α-particle energy by the 1224-keV line from the first-excited state ($9/2^-$) of ^{57}Co, while the 1223-keV line from the 14th excited state ($11/2^-$) of ^{55}Fe dominates above $E_\alpha = 60$ MeV.

Several other lines have cross-section maxima close to 100 mb, the 275-, 931-, and 1316-keV lines of ^{55}Fe from its 17th ($13/2^-$), second ($5/2^-$), and third ($7/2^-$) excited state, respectively, the 466- and 835-keV lines, dominated by ^{57}Co lines from its fourth ($11/2^-$) and 13th ($13/2^-$) excited state, respectively, the 1441-keV line from the third ($11/2^-$) excited state of ^{53}Mn, the 157- and 212-keV lines dominated by ^{54}Mn lines from its second (4^+) and third (5^+) excited states, respectively, and the 1303-keV line from the 10th (6^+)

excited state of ^{56}Fe. This list of the strongest lines shows a clear tendency for α-particle reactions with Fe to preferably populate states with spins above $J = 3$. A good illustration is the strong population of the cascade with the 275-, 605-, 1223-, and 1316-keV lines of ^{55}Fe, starting with the $J^\pi = 15/2^-$ state at 3.419 MeV.

For all of these lines and several others with cross-section maxima around 50 mb, cross sections have been determined. They are presented in Table VII. At lower α-particle energies, several relatively strong lines from ^{58,59}Ni and ^{58,59}Co isotopes have been measured by Seamster *et al.* [23] and Belhout *et al.* [10], which are not included in the list. Cross sections for those lines could not be determined in this work, because they were weak and sometimes also blended in with nearby stronger lines, without the possibility to extract meaningful line integrals.

With the exceptions of line complexes around 1.23 and 1.42 MeV, where the determination of line integrals needed some lineshape calculations, line integrals in HP-Ge spectra could be determined by simple peak fitting using the RadWare software [24], which is optimized for the analysis of HP-Ge detector spectra. Data from the LaBr$_3$ detector could only be obtained for about half of the lines, and needed in most cases

TABLE VI. γ-ray lines in α-particle reactions with the Si target for which cross sections have been obtained. The first column designs the energy of the γ-ray line or the approximate mean energy of the line complex. Lines listed in the third column were either necessary for the lineshape analyses or have non-negligible contributions (above the few-percent level of the total line content) in TALYS calculations. See Supplemental Material [25] for numerical values of the cross sections.

E_{line} (keV)	Main component	Other components	Remarks
6877	^{28}Si, 6878.79 → g.s.		
5108	^{28}Si, 6887.65 → 1779.030		
5099	^{28}Si, 6878.79 → 1779.030		
4911	^{28}Si, 6690.74 → 1779.030		
4497	^{28}Si, 6276.20 → 1779.030		
3201	^{28}Si, 4979.92 → 1779.030		
2838	^{28}Si, 4617.86 → 1779.030		
2028	^{29}Si, 2028.16 → g.s.	^{31}P 3295.0 → 1266.13	
1809	^{26}Mg, 1808.74 → g.s.		
1779	^{28}Si, 1779.030 → g.s.	^{29}Si, 3067.13 → 1273.387	
		^{25}Mg, 3405.1 → 1611.768	
		^{25}Mg, 2737.8 → 974.756	
1620	^{23}Na, 2076.011 → 439.990	^{29}Si, 3623.49 → 2028.16	Line complex
		^{20}Ne, 1633.674 → g.s.	$E =$
		^{25}Mg, 1611.768 → g.s.	1595–1652 keV
1595	^{29}Si, 3623.49 → 2028.16		
1369	^{24}Mg, 1368.672 → g.s.		
1273	^{29}Si, 1273.387 → g.s.	^{22}Ne 1274.537 → g.s.	
1265	^{30}P, 1973.27 → 708.70	^{30}Si 3498.49 → 2235.322	
		^{31}P, 1266.13 → g.s.	
1015	^{27}Al 1014.56 → g.s.	^{26}Al 2069.47 → 1057.739	
		^{26}Mg, 3941.57 → 2938.33	
440	^{23}Na, 439.990 → g.s.		
417	^{26}Al, 416.852 → g.s.		

TABLE VII. γ-ray lines in α-particle reactions with the Fe target for which cross sections have been obtained. The first column designs the energy of the γ-ray line or the approximate mean energy of the line complex. Lines listed in the third column were needed for the lineshape analysis or have non-negligible contributions (above the 5% level of the total line content) in TALYS calculations. See Supplemental Material [25] for numerical values of the cross sections.

E_{line} (keV)	Main component	Other components	Remarks
1441	^{53}Mn, 1441.15 → g.s.		
1408	^{54}Fe, 1408.19 → g.s	^{55}Fe, 1408.45 → g.s	
1316	^{55}Fe, 1316.54 → g.s		
1303	^{56}Fe, 3388.55 → 2085.1045		
1252	^{53}Mn, 2693.29 → 1441.15	^{51}Mn, 1488.15 → 237.3	
1238	^{56}Fe, 2085.1045 → 846.7778		
1223	^{55}Fe, 2539.11 → 1316.54	^{57}Co, 1223.98 → g.s.	
931	^{55}Fe, 931.29 → g.s.	^{52}Cr, 2369.630 → 1434.091	
		^{56}Fe, 5626.84 → 4700.63	
847	^{56}Fe, 846.7778 → g.s.	^{55}Fe, 2255.5 → 1408.45	
		^{54}Fe, 3793.8 → 2949.2	
835	^{57}Co, 2524.1 → 1689.6	^{53}Fe, 3175.9 → 2339.24	
		^{54}Cr, 834.855 → g.s.	
705	^{54}Mn, 1073.11 → 368.22		
605	^{55}Fe, 3419.0 → 2813.8		
576	^{56}Co, 576.50 → g.s.		
466	^{57}Co, 1689.6 → 1223.98		
411	^{54}Fe, 2949.2 → 2538.1	^{55}Fe, 411.42 → g.s.	
275	^{55}Fe, 2813.8 → 2539.11		
212	^{54}Mn, 368.22 → 156.29		
157	^{54}Mn, 156.29 → g.s	^{56}Co, 158.38 → g.s	
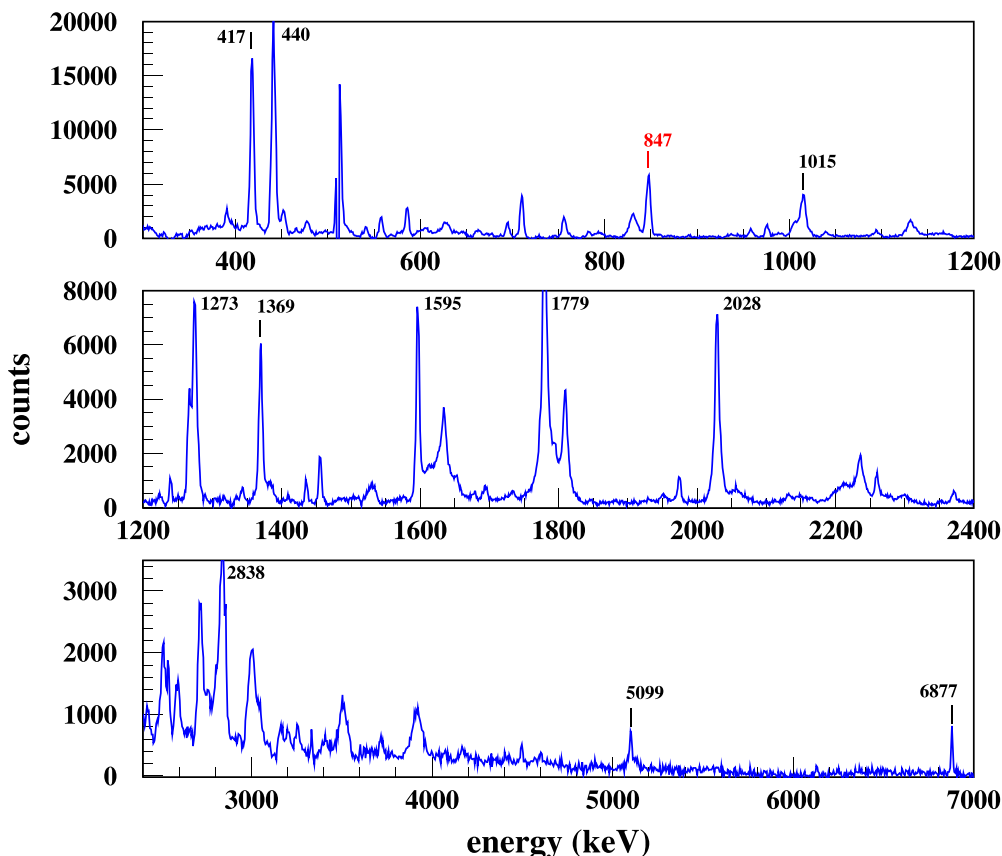
FIG. 13. Compton-suppressed spectrum of the HP-Ge detector at $\Theta = 90°$ from the irradiation of the Si target with 60-MeV α particles in the 2016 experiment in 1-keV/channel resolution below 2.4 MeV and 5-keV/channel resolution above. A selection of lines listed in Table VI are marked with their energy in keV, as well as the 847-keV line of ^{56}Fe line produced in interactions of secondary particles in the chamber walls and tubes.

lineshape calculations. Special attention had to be paid to lines of ^{56}Fe and ^{52}Cr, the major isotopes of iron and chrome that made up the stainless steel of the target chamber and the beam tubes. Lines at 847, 1238, and 1811 keV from the first three excited states of ^{56}Fe and at 936 and 1434 keV from the first

two excited states of ^{52}Cr are clearly visible in LaBr$_3$ spectra inside a band in the time-energy histograms, which is delayed by a few ns with respect to γ rays from interactions in the target (see Fig. 2). The intensity curves for these lines as a function of time show a broader secondary peak about 4 ns
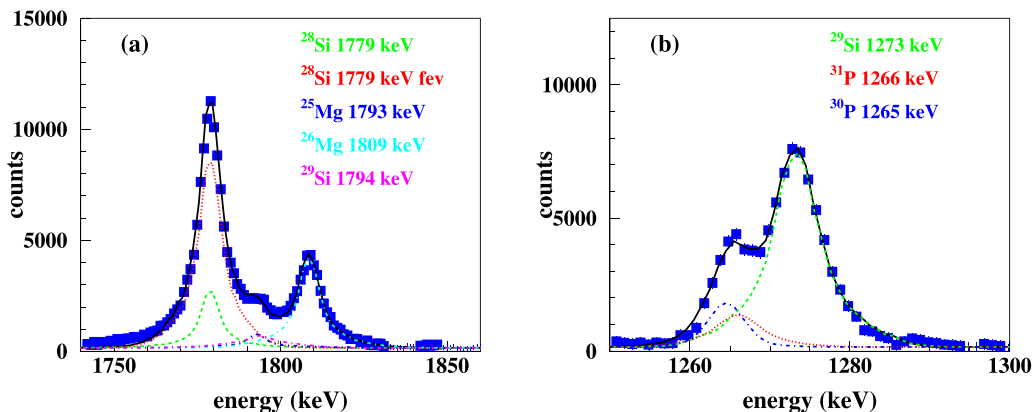
FIG. 14. Symbols show (a) the 1.78-MeV and (b) the 1.27-MeV line complexes in Compton-suppressed spectra of the Ge detector sitting at $\Theta = 90°$ for $E_\alpha = 60$ MeV. The dashed, dotted and dot-dashed lines show calculated lineshapes for the strongest components. The sum of all components is shown by the solid black lines. Two separated calculations were done for the 1779-keV line of ^{28}Si, one for the inelastic-scattering component and one for the fusion-evaporation component, labeled "fev" in panel (a).
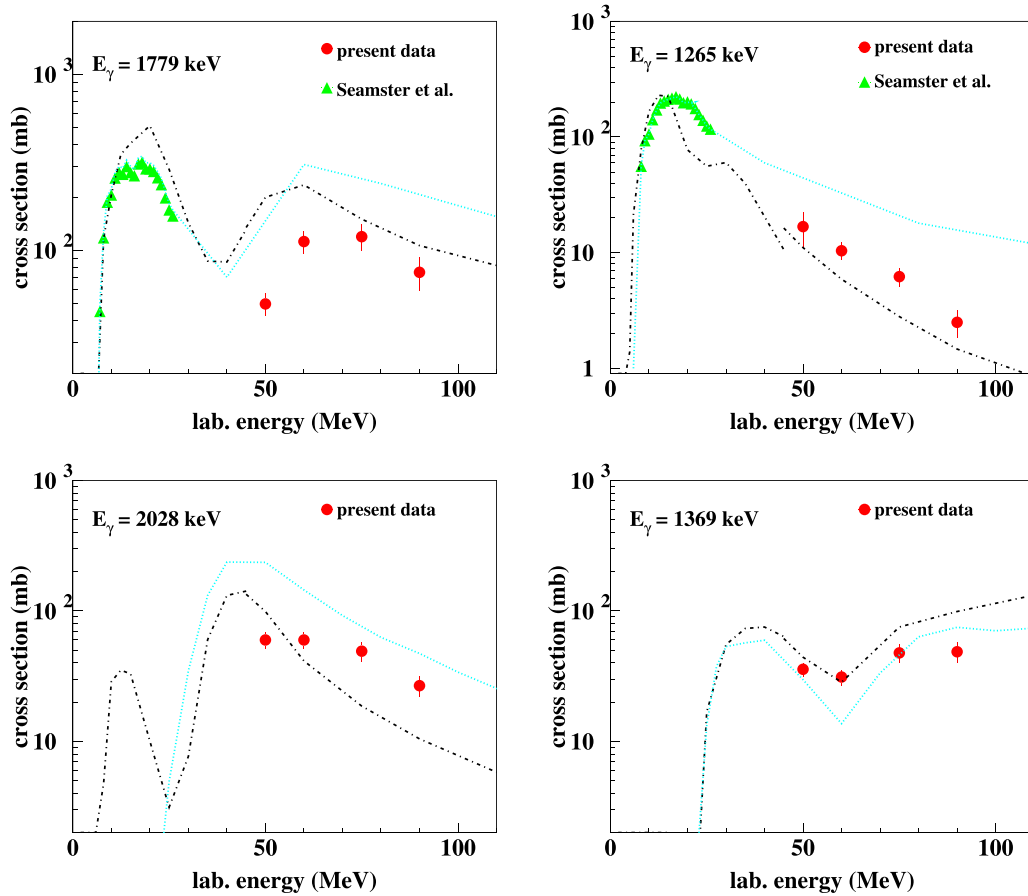
FIG. 15. Symbols show measured cross-section data for four different lines emitted in α-particle reactions with natural Si target from the present experiment, and with enriched ^{28}Si targets from Seamster *et al.* [23]. γ-ray line energies indicated in the panels refer to the lines listed in Table VI. The dotted cyan lines show the values from the cross-section compilation [4] and the dot-dashed black lines are the results of TALYS calculations. TALYS cross sections up to 45 MeV are the results for a ^{28}Si target, and above 45 MeV for a natural Si target.

later after the narrow peak from prompt target γ rays and a long decay tail extending over approximately 100 ns. This is consistent with interactions of protons and neutrons of energies about $E \approx 1.5$–10 MeV, interacting in the target chamber walls 15 cm from the target, which create the secondary peak around 4 ns, while interactions with farther away beam tubes and supporting structures are responsible for the intensity tail.

Part of these γ rays were included in the HP-Ge detector spectra, as already mentioned in Sec. III C. Their percentage was estimated and subtracted, supposing that the time structure was the same as in the LaBr$_3$ detector. This percentage depended strongly on the contour width and increased also slightly with α-particle energy in the 2016 experiment. It amounted to 17%–45% for the 847-keV line in 2016 and to 20%–65% in 2015, and to typically 10%, not exceeding 20%, for the other lines. An estimated uncertainty for this subtraction procedure was added to the uncertainty of the line integral determination, presenting therein the main source of uncertainty for the 847-keV line. The 1434-keV line of ^{52}Cr is relatively prominent at $E_\alpha = 75$–90 MeV, but the subtraction for this line was impeded by the proximity of the strong 1441-keV line of ^{53}Mn and the internal radioactivity of the LaBr$_3$ crystal. Therefore it was not included in Table VII. Other lines

that appear in this time window are at 411 and 1130 keV. They are without doubt due to the γ-ray cascade starting with the fifth excited state at 2.949 MeV in ^{54}Fe, which has a relatively long half-life of $t_{1/2} = 1.22$ ns.

Figure 17 shows cross-section data for six lines, which represent all γ-ray lines of Table VII for which there also exists data at lower α-particle energies in Refs. [10,23] or cross-section curves in the compilation of MKKS [4]. The compilation predicts correctly the shape of the second cross-section maximum for the three lines of ^{56}Fe (847, 1238, and 1303 keV), but overestimates the absolute cross sections approximately by a factor of two. It fails, however, to reproduce the curves for the lines at 1223 and 1408 keV, which for the 1223-keV line is certainly to a good part because the compilation includes only the 1224-keV line of ^{57}Co. The TALYS calculations reproduce approximately the magnitude and shape of the three ^{56}Fe lines with a shift to lower energies of the cross-section maxima and the minimum between them and slightly exaggerated amplitude. The difference between measured data and TALYS calculations below $E_\alpha \approx 10$ MeV for the 847-keV line is due to Coulomb excitation of the first excited state of ^{56}Fe, an interaction not sufficiently included in TALYS nuclear reaction calculations. For the other three lines, TALYS reproduces two of them quite correctly while it fails
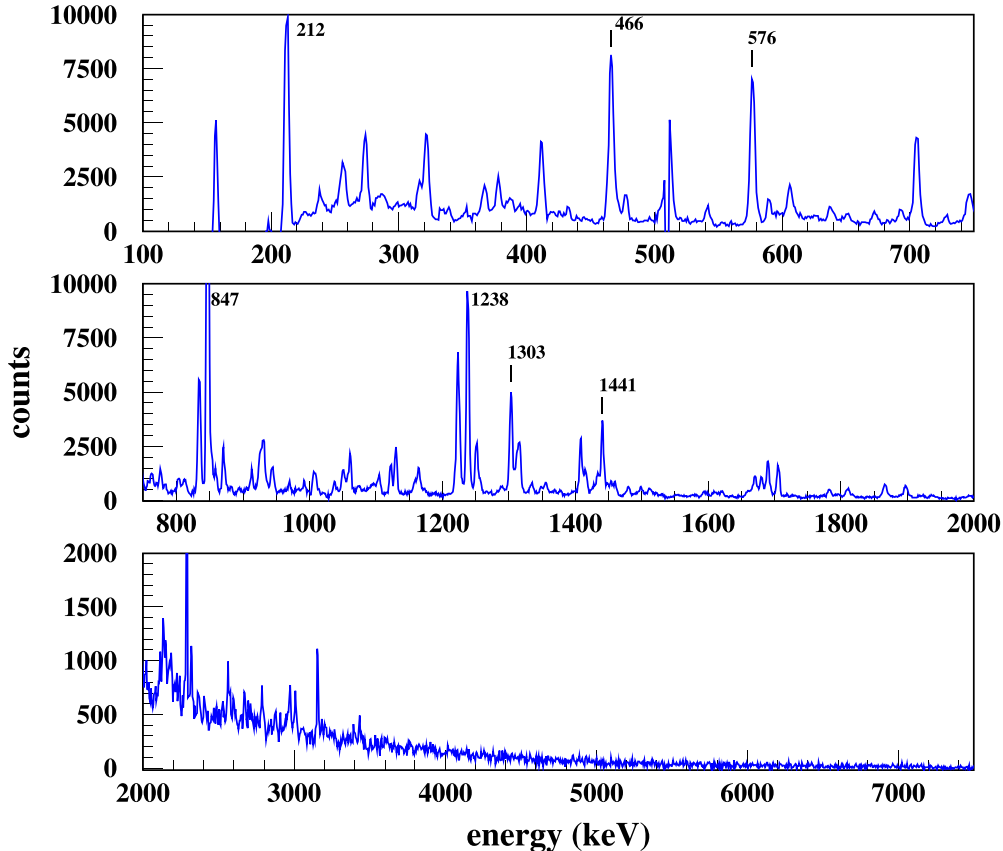
FIG. 16. Compton-suppressed spectrum of the HP-Ge detector at $\Theta = 90°$ from the irradiation of the Fe target with 60-MeV α particles in the 2016 experiment in 1-keV/channel resolution below 2.0 MeV and 5-keV/channel resolution above. A selection of lines listed in Table VII are marked with their energy in keV.

completely for shape and magnitude of the 1408-keV line. These examples are representative also for the other lines of Table VII.

Only five γ-ray lines out of eighteen in the list of Table VII have cross-section curves for α-particle-induced reactions in the cross-section compilation MKKS [4]. On the other side, there are 14 other lines in MKKS with relatively high cross sections at lower α-particle energies, which were too weak in the currently explored range $E_\alpha = 50$–90 MeV for cross-section determinations. Addition of the present data to the compilation would therefore represent a comprehensive data set of cross sections for about 30 of the strongest lines for α-particle reactions with Fe below $E_\alpha = 90$ MeV. Because many of the lines, however, have data either below 40 MeV only or above 50 MeV, extrapolations to higher or lower energies are still required. These should be guided by nuclear reaction calculations, like the TALYS calculations with default parameters presented here. The rich γ-ray cross-section data set existing now for α + Fe should allow us to optimize parameters in TALYS calculations for an accurate description of the data and improvement of the extrapolations.

V. SUMMARY

New γ-ray line production cross sections for α-particle reactions with C, Mg, Si, and Fe have been determined in two experiments at the Helmholtz-Zentrum Berlin. Data for about 60 different γ-ray lines at $E_\alpha = 50$, 60, 75, and 90 MeV could be obtained and compared with the curves of the most recent compilation for strong γ-ray emission lines in solar flares and with predictions of a modern nuclear reaction code. The predicted second, broad cross-section maxima for deexcitation lines from the first few excited states of the major target isotopes ^{12}C, ^{24}Mg, ^{28}Si, and ^{56}Fe have been observed, however, in most cases they are much weaker than in the compilation and the reaction code calculations.

More generally, the compilation and the nuclear reaction code calculations agreed only modestly with the measured data for many of the lines, showing the need for experiments to obtain reliable γ-ray cross-section data. This disagreement between actual data and calculations has been studied more in detail for the 4.439-MeV line of ^{12}C, showing that an important part was due to a strong underestimation of the inelastic-scattering component in the reaction code calculations. A significant improvement could be obtained by adjusting the nuclear reaction potential in the reaction code for α-particle scattering off ^{12}C. The potential was determined by reproducing a set of inelastic-scattering angular distribution data in coupled-channels calculations. Lineshape calculations for the 4.439-MeV line of ^{12}C, based on the same coupled-channels calculations were also done and they reproduced
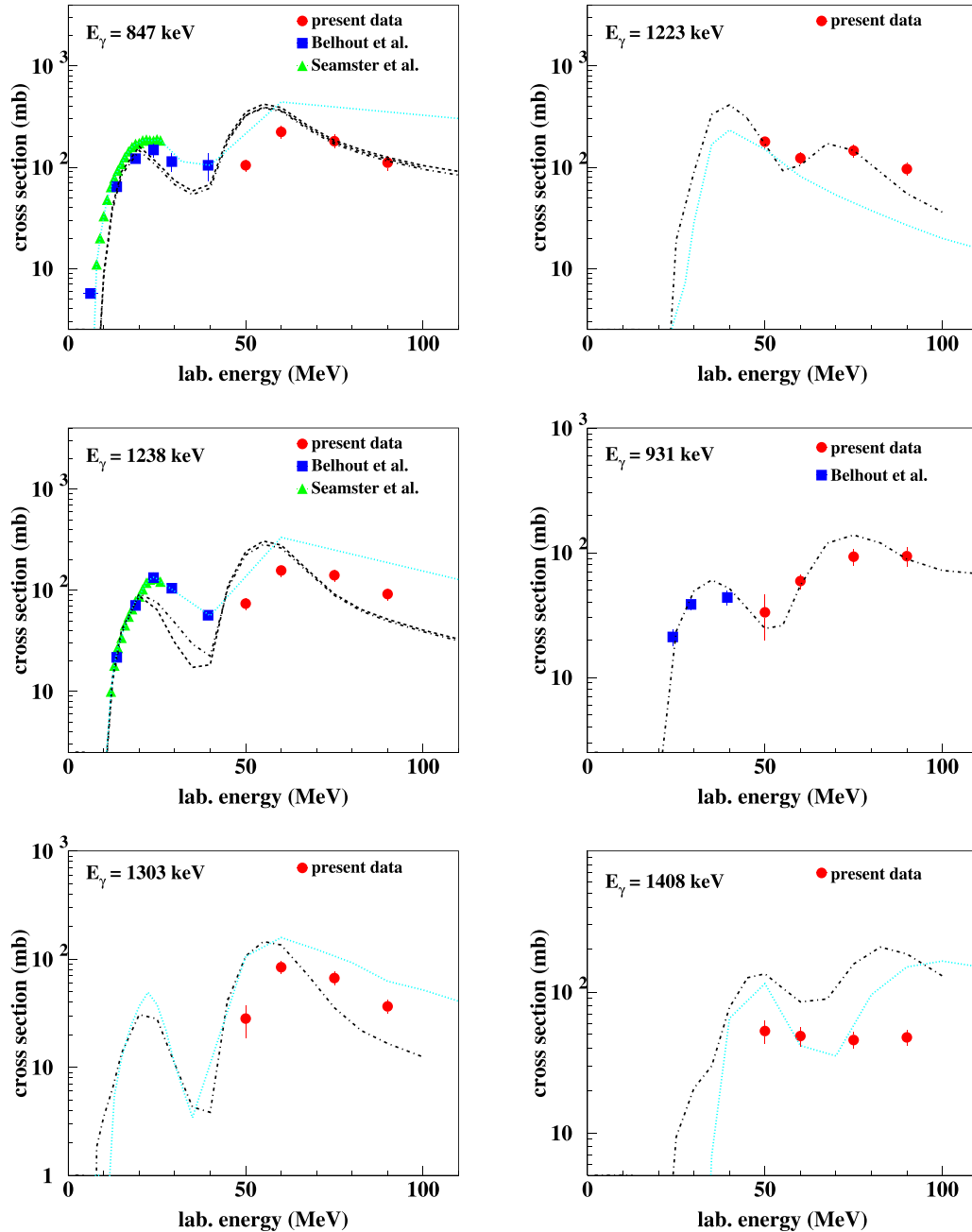
FIG. 17. Symbols show measured cross-section data for six different lines emitted in α-particle reactions with natural Fe target from the present experiment and from Belhout *et al.* [10], and with enriched ^{56}Fe targets from Seamster *et al.* [23]. γ-ray line energies indicated in the panels refer to the lines listed in Table VII. The dotted cyan lines show the values from the cross-section compilation [4] and the black lines are the results of TALYS calculations, dashed for enriched ^{56}Fe target and dot-dashed for natural Fe target.

accurately the lineshapes measured with high-resolution Ge detectors.

With the present data the accuracy of the cross-section data base for many strong γ-ray lines produced in astrophysical sites with accelerated-particle populations could be significantly improved in an important energy range for α-particle reactions. For all of the strongest lines of the major target isotopes of C, Mg, Si, and Fe, data exist now from reaction threshold to 90 MeV α-particle energy and

can be used directly in astrophysical and other applications. In, e.g., typical solar flares with accelerated-particle energy distributions following a power law in kinetic energy with E^{-s} ($s = 3.5$), more than 98% of the strong γ-ray line emission induced by α-particle reactions is produced in this energy range. This means that a practically complete coverage with experimental data is obtained with the present results. Before this work, experimental data for most of the strong lines existed only below

$E_\alpha \approx 26$–37 MeV, covering about 85%–95% of the emission in a typical flare.

Extrapolations to higher energies for sites with a much harder particle energy spectrum and cross-section data for weaker lines need probably detailed analyses of the parameters in nuclear reaction code calculations. For that purpose, there is now an important data base for γ-ray emission cross sections, which can be complemented, as illustrated for the $\alpha + {}^{12}$C reaction, by other data like differential elastic and inelastic scattering and transfer cross sections. Eventually, such γ-ray cross-section data can also be used for other applications with energetic particles, such as, for example, in hadron therapy. In any case, the present results underline the importance of measurements at particle accelerators for the establishment of an accurate cross-section data base in a wide projectile energy range.

[1] R. Ramaty and G. M. Simnett, in *The Sun in Time*, edited by C. P. Sonett, M. S. Giampapa, and M. S. Matthews (The University of Arizona Press, Tucson, 1991), pp. 232–259.

[2] R. Ramaty, B. Kozlovsky, and R. E. Lingenfelter, Astrophys. J., Suppl. Ser. **40**, 487 (1979).

[3] B. Kozlovsky, R. J. Murphy, and R. Ramaty, Astrophys. J., Suppl. Ser. **141**, 523 (2002).

[4] R. J. Murphy, B. Kozlovsky, J. Kiener, and G. H. Share, Astrophys. J., Suppl. Ser. **183**, 142 (2009).

[5] A. J. Koning, S. Hilaire, and M. C. Duijvestijn, in *TALYS-1.0, Proceedings of the Int. Conf. on Nuclear Data for Science and Technology, April 22-27, 2007, Nice, France* (EDP Sciences, Les Ulis, 2008), p. 211.

[6] https://www.fastcomtec.com.

[7] https://gepool.in2p3.fr/.

[8] R. Brun and F. Rademakers, ROOT — An object oriented data analysis framework, Nucl. Instrum. Methods Phys. Res. A: Accel. Spectrom. Detect. Assoc. Equip. **389**, 81 (1997).

[9] S. Agostinelli, J. Allison, K. Amako, J. Apostolakis, H. Araujo *et al.*, Nucl. Instrum. Methods Phys. Res., Sect. A **506**, 250 (2003).

[10] A. Belhout, J. Kiener, A. Coc, J. Duprat, C. Engrand *et al.*, Phys. Rev. C **76**, 034607 (2007).

[11] P. Dyer, D. Bodansky, D. D. Leach, E. B. Norman, and A. G. Seamster, Phys. Rev. C **32**, 1873 (1985).

[12] G. F. Burdzik and G. Heymann, Nucl. Phys. A **185**, 509 (1972).

[13] N. Baron, R. F. Leonard, and W. M. Stewart, Phys. Rev. C **4**, 1159 (1971).

[14] T. Mikumo, J. Phys. Soc. Jpn. **16**, 1066 (1961).

[15] N. N. Pavlova and A. V. Yushkov, Yad. Fiz. **23**, 252 (1976).

[16] J. Raynal, Note CEA **N-272** (1994).

[17] J. Kiener, Phys. Rev. C **99**, 014605 (2019).

[18] M. Yasue, T. Tanabe, F. Soga, J. Kokame, F. Shimokoshi *et al.*, Nucl. Phys. A **394**, 29 (1983).

[19] A. D'Arrigo, G. Fazio, G. Giardina, O. Y. Goryunov, A. P. Ilyin *et al.*, Nuovo Cimento A **107**, 1353 (1994).

[20] P. D'Agostino, G. Fazio, G. Giardina, O. Y. Goryunov, M. Sacchi *et al.*, Nucl. Phys. A **583**, 437 (1995).

[21] W. Yahia-Cherif, S. Ouichaoui, J. Kiener, V. Tatischeff, E. A. Lawrie, J. J. Lawrie, V. Tatischeff, A. Belhout, D. Moussa, P. Papka *et al.*, Phys. Rev. C **102**, 025802 (2020).

[22] Reed, Ph.D. thesis: Reed, 69-14 (1968), data available at https://www-nds.iaea.org/exfor/exfor.htm

[23] A. G. Seamster, E. B. Norman, D. D. Leach, P. Dyer, and D. Bodansky, Phys. Rev. C **29**, 394 (1984).

[24] D. C. Radford, Nucl. Instrum. Methods Phys. Res., Sect. A **361**, 297 (1995).

[25] See Supplemental Material at http://link.aps.org/supplemental/10.1103/PhysRevC.104.024621 for numerical values of the cross sections and it contains files (aC.data, aFe.data, aMg.data and aSi.data) which are in ASCII format, as well as an file explaining the data format in these files.